
CHAPTER 8: TRAPPING ELECTROCHEMICAL OSCILLATIONS BETWEEN SELF-ORGANIZED POTENTIAL WALLS

In chapter 6 the effect of the ohmic drop compensation upon the stability of uniform electrode states was discussed. It was argued that, among other advantages, the use of an electronic device for partially compensating the ohmic drop through the electrolyte could opening the possibility of exploring the effect of stronger negative global coupling on pattern formation in electrochemical systems. Following the systematic studies on the impact of the

NGC on the pattern formation in the oscillatory $\text{Pt}|\text{H}_2\text{SO}_4, \text{Cl}^-, \text{Cu}^{2+}|\text{H}_2$ system, in this chapter results obtained under strong NGC are reported. Besides the traveling pulse pattern already mentioned in chapters 6 and 7, which is a well known manifestation of the NGC, the observation of spatiotemporal oscillations that are trapped inside self-organized potential walls are reported [212]. The presented results were obtained in the parameter region already mentioned in the R_c/R_Ω versus U diagram shown in chapter 7.

In the first section, an overview of the different potential regions in which spatiotemporal patterns were observed is presented. In the following section, the first region in which traveling pulses were observed is studied. Then, the existence of self-organized potential walls in the bistable $\text{Pt}|\text{H}_2\text{SO}_4|\text{H}_2$ system is discussed as a bridge for the next section dealing with the observation of oscillatory spatial domains trapped inside such potential walls. Finally, the main results are summarized.

8.1 OVERVIEW

A general view of the studied system is given in Figure 8.1, which shows two cyclic voltammograms recorded at 0.05 V s^{-1} . The external RE was used in both cases, and in curve *i* the uncompensated resistance, R_u , is the same as the cell resistance and amounts to $540 \pm 10 \Omega$. In curve *ii* the NID was employed and R_{NID} was set to -350Ω , such that $R_u = 180 \pm 10 \Omega$ and $R_c/R_\Omega \approx 0.65$. The general dynamic features of the system given in curve *i* are very similar to the ones shown in Figure 6.5 since for this configuration (i.e., the CE placed between the RE and the WE) no NGC is induced. Besides the evident effect of the compensated resistance on the shape of curves *i* and *ii*, the oscillatory dynamics change dramatically between these two curves. When partially compensating the ohmic drop through the electrolyte as done in curve *ii*, two main differences are observed in the current oscillations during the positive scan. The first concerns the form of the current oscillations in a similar way as discussed in chapter 6. For $R_c \neq 0$ they are less regular (curve *ii*). The second feature differentiating curve *ii* is the presence of a broader region mediating the active (high current)/passive (low current) transition close to the positive potential turning point in contrast to the steep transition observed in curve *i*.

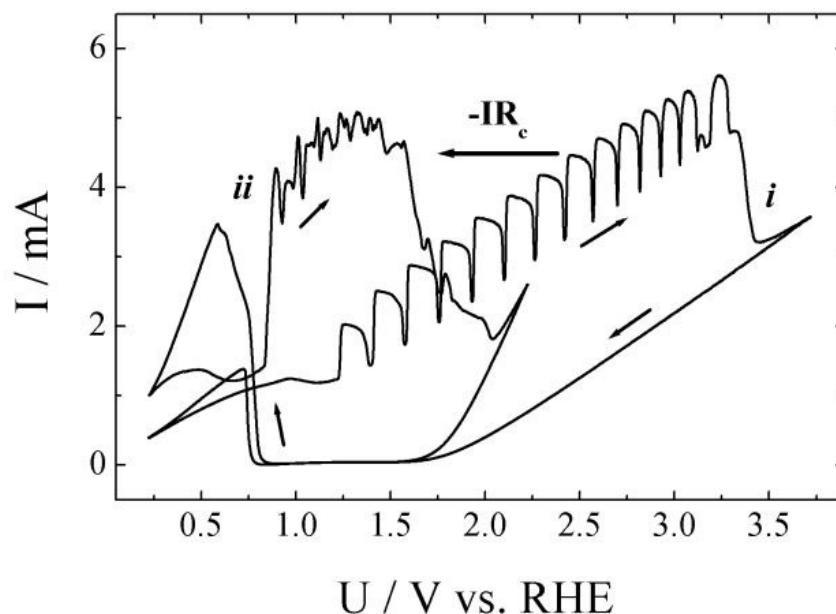


Figure 8.1: Cyclic voltammogram at 0.05 Vs^{-1} for the $\text{Pt}|\text{H}_2\text{SO}_4, \text{Cl}^-, \text{Cu}^{2+}|\text{H}_2$ system. In curve *i* $R_u (= R_\Omega) = 540 \pm 10 \Omega$, and curve *ii* $R_u = 180 \pm 10 \Omega$ ($R_c = -R_{\text{NID}} = 350 \Omega$), see text for details. Electrolyte: 0.5 mM H_2SO_4 , 0.1 mM HCl , and 0.05 mM CuSO_4 saturated with H_2 . Rotation rate of the electrode $\omega = 20 \text{ Hz}$.

A closer examination of the different oscillatory regions during the cycling is displayed in Figure 8.2 which shows in plate (a) the voltammetric behavior at 0.01 Vs^{-1} for the system under similar conditions as shown in curve *ii* in Figure 8.1. Figures 8.2 (b), (c) and (d) show the spatiotemporal evolution of the interfacial potential in front of the ring WE obtained during the voltammetric sweep shown in plate (a) in three selected regions.

Similarly to the cyclic voltammogram in Figure 8.1 (curve *ii*), the CV in Figure 8.2 (a) shows a sharp increase in current at ca. 0.8 V during the positive scan, concomitantly to the onset of oscillations. Upon further increasing the applied voltage, the current slightly increases, attaining its upper limit of about 4.8 mA at 1.12 V. The current plateau persists up to ca. 1.38 V. This oscillatory window is identified as region *I*. As displayed in Figure 8.2 (b), this region is characterized by the presence of traveling pulses. In this case the amplitude of the pulses amounts to about 0.40 V, and the interfacial potential stays always well below the value at which oxide formation sets in. Thus, in region *I* the observed pattern are caused by the oscillations in the HN-NDR-type of oscillator of the $\text{Pt}|\text{H}_2\text{SO}_4, \text{Cl}^-, \text{Cu}^{2+}|\text{H}_2$ system just as in the other cases investigated so far in chapters 5 to 7.

The second pattern forming window is found on the shoulder mediating the active/passive transition (region 2). Throughout this region the electrode is partially covered by platinum oxide, and the oscillatory HOR is confined inside the remaining active domain as fairly seen in Figure 8.2 (c). This figure shows the nucleation and growth of a passive domain (yellow/red) in an active background (blue/green), the coexistence of active and passive domains along the voltage scan is characterized by the presence of spatial structures trapped inside the passive borders or potential walls. In contrast to the patterns observed in region 1, the emergence of patterns in region 2 results from the interplay between the bistable dynamics of the N-NDR, $\text{Pt|H}_2\text{SO}_4|\text{H}_2$ system, and the oscillatory $\text{Pt|H}_2\text{SO}_4, \text{Cl}^-, \text{Cu}^{2+}|\text{H}_2$ system. The spatiotemporal evolution of the interfacial potential during the passive to active transition observed throughout the backward scan starting at around 0.9 V is displayed in Figure 8.2 (d).

Regions 1 and 2 displayed in Figure 8.2 will be separately analyzed in potentiostatic experiments, whereas the third region corresponding to the passive to active transition shown in Figure 8.2 (d) will not be further investigated.

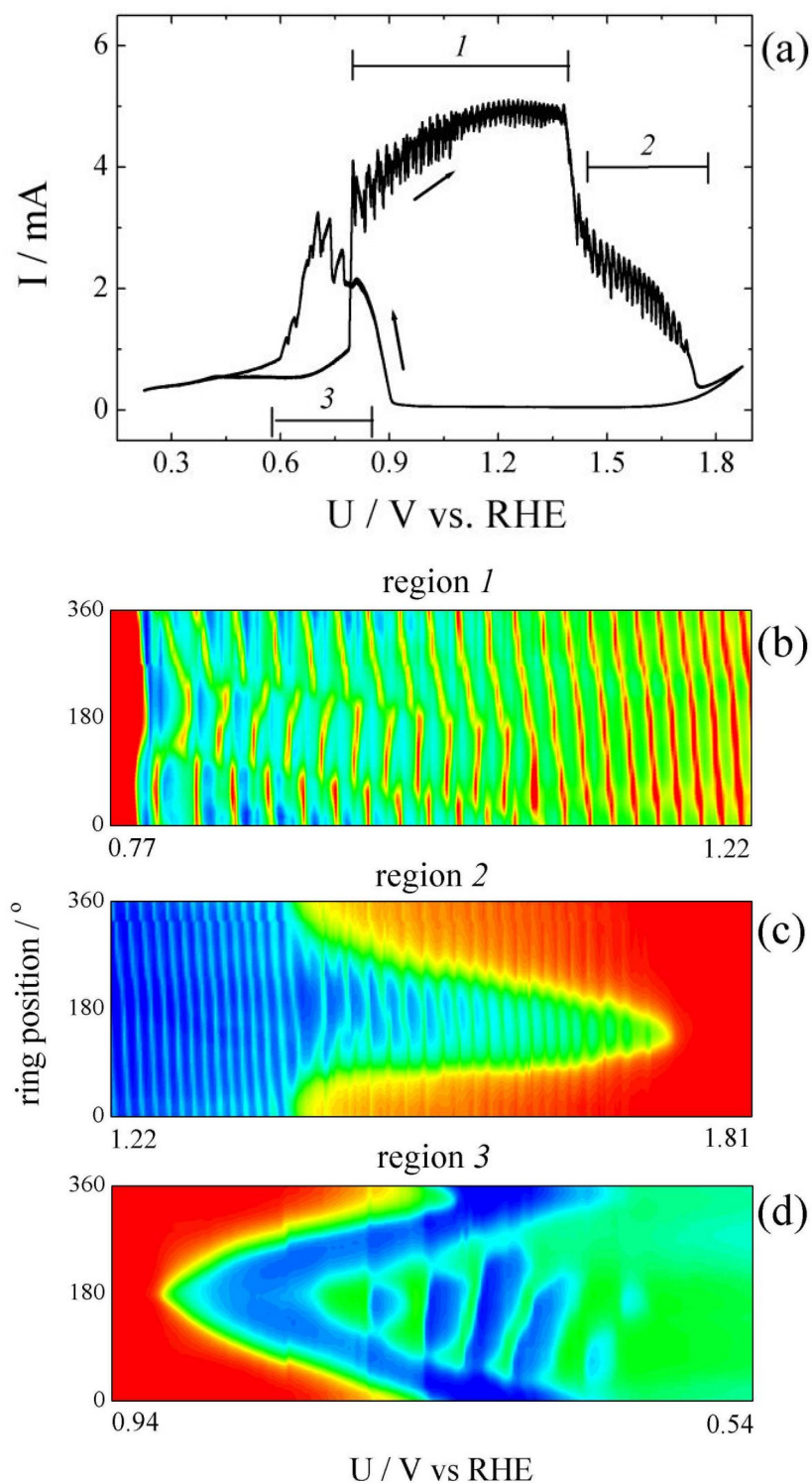


Figure 8.2: (a): Cyclic voltammogram under conditions similar to those underlying curve *ii* in Figure 8.1 but at 0.01 Vs^{-1} . (b), (c), and (d): Spatiotemporal evolution of the interfacial potential $U_{PP}(x,t)$ obtained during the voltammetric scan shown in plate (a) corresponding to regions 1, 2, and 3. The color scale in these plot goes from blue to red in the following range: (a) 0.10 to 0.55 V, (b) 0.40 to 1.70 V, and (c) 0.15 to 0.90 V.

8.2 TRAVELING PULSES

Stationary experiments at different values of the applied voltage were carried out in order to investigate the patterns existing in region 1 (Figure 8.2 (b)) in more detail. Typical traveling pulses observed at different value of the applied voltage are shown in Figure 8.3. Displayed is the inhomogeneous part of the interfacial potential together with the corresponding time series of the global current oscillations.

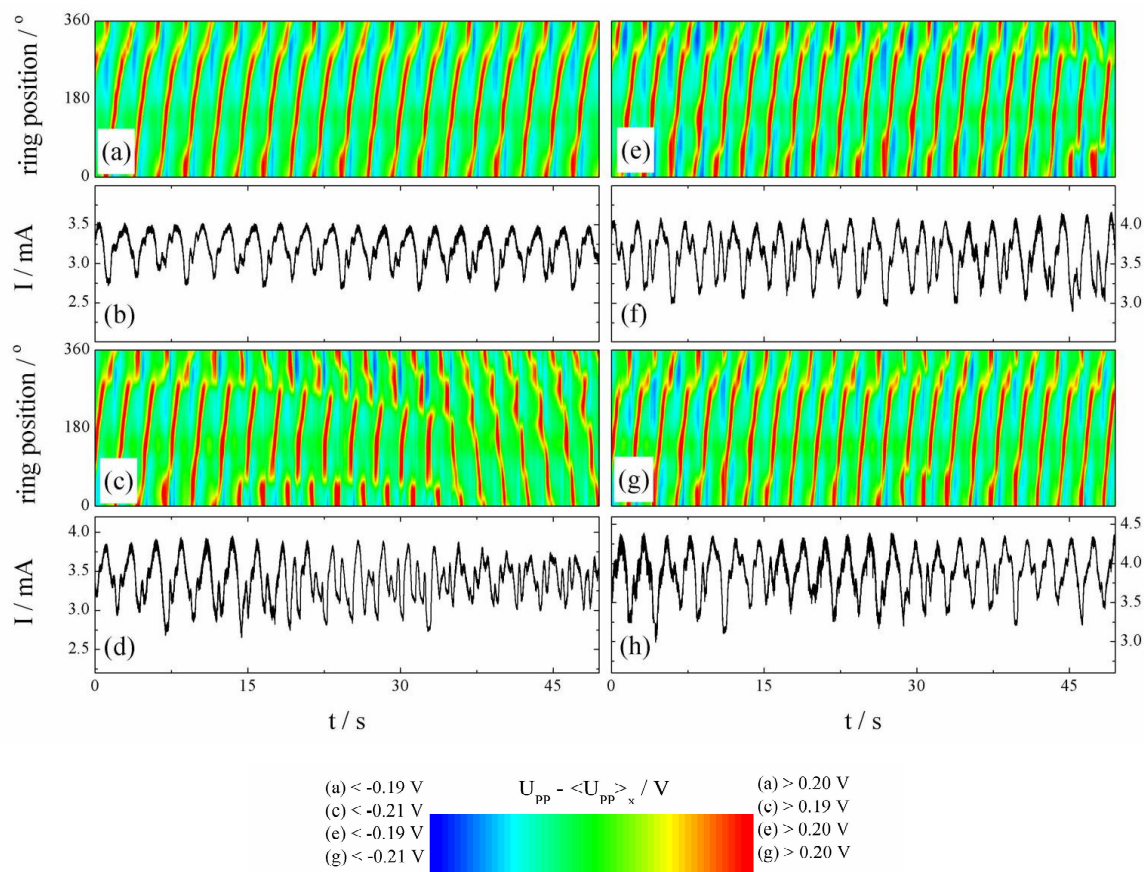


Figure 8.3: (a), (c), (e), and (g): Spatiotemporal evolution of the inhomogeneous part of the interfacial potential, $U_{PP}(x) - \langle U_{PP} \rangle_x$, as a function of the ring position and time. (b), (d), (f), and (h): the corresponding current time series. Applied voltage: (a) and (b) 0.79 V; (c) and (d) 0.84 V; (e) and (f) 0.89 V; (g) and (h) 0.94 V. Remaining conditions as in Figure 8.1 (b). In all space-time plots the same position of the electrode was chosen as 0° .

All global current-time traces shown in Figure 8.3 are qualitatively similar. They oscillate around the value of the current plateau (cf. Figure 8.2 (a)) with amplitudes of about 1 mA. In all spatiotemporal plots shown in Figure 8.3 the pulse propagation occurs from small to larger angular positions with the exception of the case shown in plate (c) in which after a short transient the pulse spontaneously changes its propagation direction.

As anticipated in chapter 6, the oscillations in the global current result from changes in the pulse width (modulations) during the propagation of the pulse along the ring electrode, since perfect, unmodulated pulses would imply that the current density is constant. In the plots shown in Figure 8.3 the observed current maximum during each oscillation corresponds to a decrease in the pulse width or even to a propagation failure of the pulse. This behavior has been related [47] to an inhomogeneity of the electrode. Hence, the current oscillations could be the result of a change of the local activity of the electrode. Focusing on Figure 8.3 (a) for instance, the pulse slows down whenever it reaches a position around 300° . When analyzing the remaining space-time plots, however, it becomes clear that this interpretation is oversimplified. As clearly seen in Figure 8.3 (c), in the region in which the pulse slowed down in Figure 8.3 (a) a ‘point of propagation failure’ develops. This defect region is not stationary but begins to move towards the central ring position and seems to disappear or split into two different points at ca. 35 s. With time also another point of propagation failure is born at about 60° and 14 s which lives until $t = 35$ s (see also Figure 8.2 (b)). Figure 8.4 shows a blow up of this region.

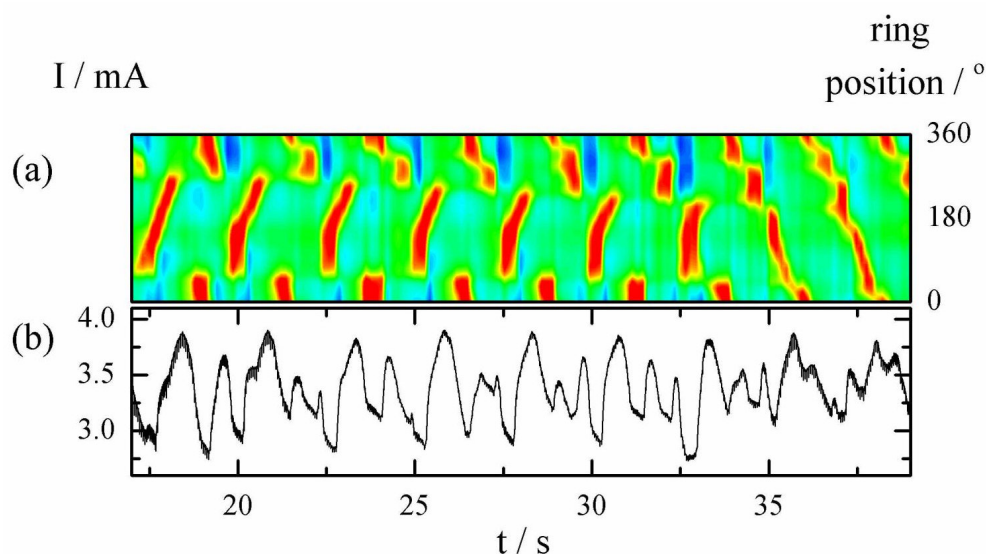


Figure 8.4: Selected region taken from Figures 8.3 (c) and (d). Color scale and the remaining parameters as in Figure 8.3.

In fact, the behavior displayed in Figure 8.4 (a) is closer to a cluster-like pattern than to a traveling pulse. Furthermore, the cluster-like structures mediate the transition of the direction in which the pulse propagates along the ring.

It should be emphasized that, although the described points of propagation failure seem to be predominantly at two particular positions, namely around 60° and 300° , they were not really stationary and, therefore, no explicit relation between the pulse propagation and specific points on the ring could be obtained. However, although pulse modulation and propagation failure are not directly pinned to the presence of surface non-uniformities, it cannot be excluded that slight variations in the catalytic properties of the ring WE can still present an intricate interaction with the self organized pattern.

As far as ‘real surfaces’ are concerned, non-uniformity is up to some extent unavoidable and can occur on scales of several orders of magnitude. In heterogeneous reactions non-uniformities are usually associated to surface defects, such as small domains with enhanced step density or enhanced density of impurity atoms randomly distributed at the surface [17, 18], for example. Modulated pulses and rather similar ‘cluster-like’ motions during complex back-and-forth pulse propagation have been observed by Luss and coworkers in the atmospheric oxidation of hydrogen on a nickel ring [213]. In this case, however, the presence of non-uniformities has been clearly addressed by the authors as a result of catalyst aging [213]. The question of how the self-organized patterns interact with non-uniformities is of key relevance [15, 214-218]. Non-uniformity detection, characterization, and evolution under experimental conditions are considered very difficult questions when dealing with reacting media.

Although indirect, an additional evidence that the observed behavior constitutes an intrinsic dynamic feature of the system rather than a result of some non-uniformity along the ring results from recent numerical simulations under strong NGC conditions carried out by Plenge [129]. Using a spatially extended version of the realistic homogeneous model already mentioned in chapter 2 [53], the author captured some typical modulated pulse patterns including points of propagation failure without assuming any surface non-uniformity [129]. Important in the present context is the fact that no perfect (unmodulated) pulses were observed at all in the simulations. As an example, consider the simulated spatiotemporal evolution of the interfacial potential and the global current shown in Figure 8.5.

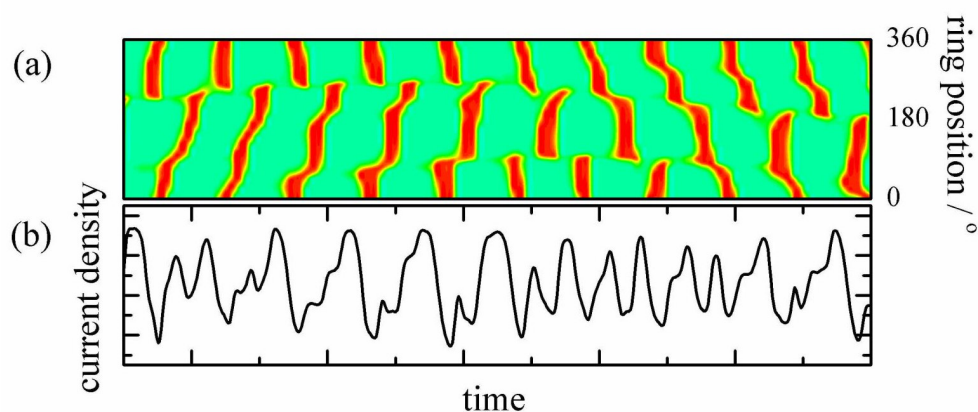


Figure 8.5: Simulated spatiotemporal evolution of the interfacial potential, as well as its global current time series. The model is a spatially extended version of the one describing the oscillatory dynamics of the HOR in the presence of Cl^- and Cu^{2+} and mentioned in chapter 2[53]. In this example $R_c/R_\Omega = 0.90$. For details see ref. [129].

This particular result was obtained for $R_c/R_\Omega = 0.90$ in a parameter region close to the one where modulated pulses were observed. Plenge referred to this pattern as an irregular type of asymmetric target pattern [129]. Note the resemblance with the experiments shown above in Figure 8.4.

Pulses are a common coherent structure formed in one-dimensional systems [49, 51]. Traveling pulses on annular geometry have been extensively observed in heterogeneous catalyzed reactions, such as the reduction of nitrogen monoxide with carbon monoxide on platinum [219] or hydrogen oxidation on nickel [15, 22, 213]. In electrochemical systems, traveling pulses were first observed by Jaeger's group during cobalt electrodisolution [45, 144] and later on in other systems, such as the formic acid electrooxidation [43, 148, 150, 187] and also during the HOR in the presence of Cl^- and Cu^{2+} as studied here [47].

Traveling pulse solutions may result from the action of global coupling in oscillatory systems. In heterogeneous catalyzed reactions, for instance, the global constraint can be provided by the temperature control of the catalyst [220-224]. In electrochemical environment, the occurrence of pulses is primarily caused by the NGC that stabilizes the homogeneous mode, but not the spatially inhomogeneous modes. Owing to the rotational invariance of the one-dimensional annular spatial domain, the eigenfunctions are Fourier modes, whereby sine and cosine modes are degenerated and become unstable simultaneously. Therefore, the observed traveling pulses results from a simultaneous excitation of these two

inhomogeneous modes with lowest wave numbers [47, 78]. Another very common manifestation of the NGC in reaction-migration systems is the observation of standing wave patterns where only one of the two degenerated inhomogeneous modes is excited [42, 43, 78, 187]. In any case, the desynchronizing feature of the NGC leads to an inherent anti-phase-like dynamics, and it can prevent the electrode surface from undergoing complete poisoning since the existence of passive regions implies the activation of opposite regions.

8.3 STATIONARY POTENTIAL WALLS IN THE BISTABLE $\text{Pt}|\text{H}_2\text{SO}_4|\text{H}_2$ SYSTEM

The first step towards the understanding of the structures shown above in Figure 8.2 (c), region 2, is to understand the nature of the potential walls. These walls are already observed in the bistable $\text{Pt}|\text{H}_2\text{SO}_4|\text{H}_2$ system in the presence of strong NGC (s.b.). Figure 8.6 shows the current/voltage curves under potentiodynamic control in the $\text{Pt}|\text{H}_2\text{SO}_4|\text{H}_2$ system during the active/passive transition.

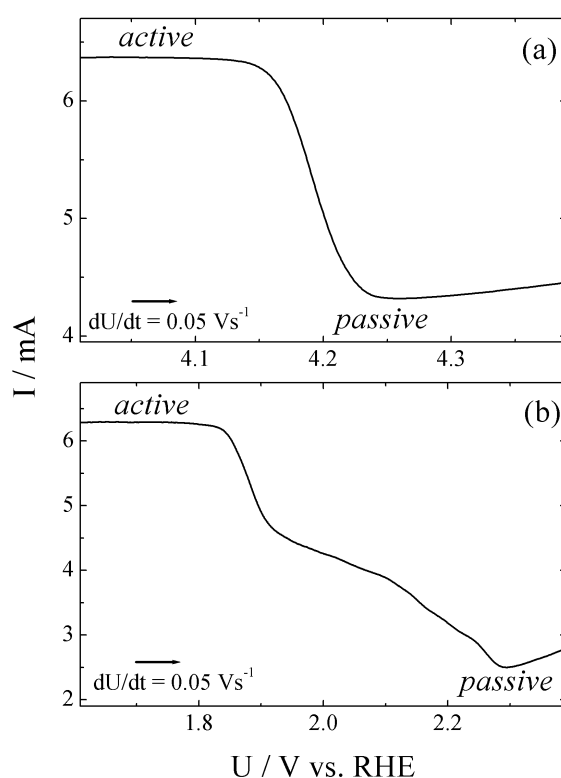


Figure 8.6: Current/voltage curves during the potentiodynamically driven (0.05 Vs^{-1}) active/passive transition for the $\text{Pt}|\text{H}_2\text{SO}_4|\text{H}_2$ system. (a) $R_u (= R_\Omega) = 580 \pm 10 \Omega$ and (b) $R_u = 230 \pm 10 \Omega$ ($R_c = -R_{\text{NID}} = 350 \Omega$). Electrolyte: $0.5 \text{ mM H}_2\text{SO}_4$ saturated with H_2 . Rotation rate of the electrode $\omega = 20 \text{ Hz}$.

Plates (a) and (b) were obtained under conditions equivalent to those in Figure 8.1, curve *i*: in Figure 8.6 (a) $R_u (= R_\Omega) = 580 \pm 10 \Omega$, and therefore no NGC is present; in Figure 8.6 (b), however, the NID was employed ($R_c = -R_{\text{NID}} = 350 \Omega$) and $R_c/R_\Omega \approx 0.6$. The current levels of the active state are identical in both cases, and the differing current at the passive states is due to the oxygen evolution reaction, which proceeds in the two cases at different rates because of the different interfacial potentials. The most remarkable difference between the two I/U curves in Figure 8.6 is the current shoulder mediating the active/passive transition in (b), which is also present in region 2 in Figure 8.2 (a). In the absence of the destabilizing NGC, transitions between active and passive states are mediated by a monotonic current decrease as a result of the nucleation and growth of the globally stable phase upon changing the control parameter U . The NGC may stabilize a patterned state at the electrode surface in which the two states are simultaneously present. As can be seen in Figure 8.6 (b), the active/passive transition becomes broader under these conditions, and the current attains values between those of the active and passive state reflecting the existence of a patterned state in which the passive phase occupies only part of the annulus and native platinum area is still available for the HOR.

The influence of the NGC on the active/passive and passive/active transitions in the bistable $\text{Pt}|\text{H}_2\text{SO}_4|\text{H}_2$ system has been studied in detail by Grauel and Krischer [41]. For the strongest NGC studied (that is, R_c/R_Ω near 0.4) the emergence of stationary structures comprising free and oxide-covered platinum domains were found during both active/passive and passive/active transitions. Figure 8.7 shows an example in which an autonomous transition from a reactive to a patterned state takes place at a constant applied voltage [41]. Current density, i , and interfacial potential, U_{PP} , as a function of time are shown in plates (a) and (b), respectively, whereas two snapshots of U_{PP} as a function of the ring position are presented in plate (c).

As is seen in the current trace in Figure 8.7 (a), the spontaneous nucleation of the passive state occurs at about 11 s and it grows up to c.a. 45 s. From this time on the current stays nearly stationary at a value of 2.7 mA. The evolution of an interfacial pattern can be anticipated from the large amplitudes U_{PP} exhibits during one rotation of the ring electrode. Two profiles of U_{PP} along the ring are shown in Figure 8.7 (c). The first curve (closed circles) shows a transient state at 14 s where the oxide-covered phase is still expanding. The second

curve (open circles) depicts the fully developed stationary profile. Here the passive domain covers about 80 % of the electrode surface.

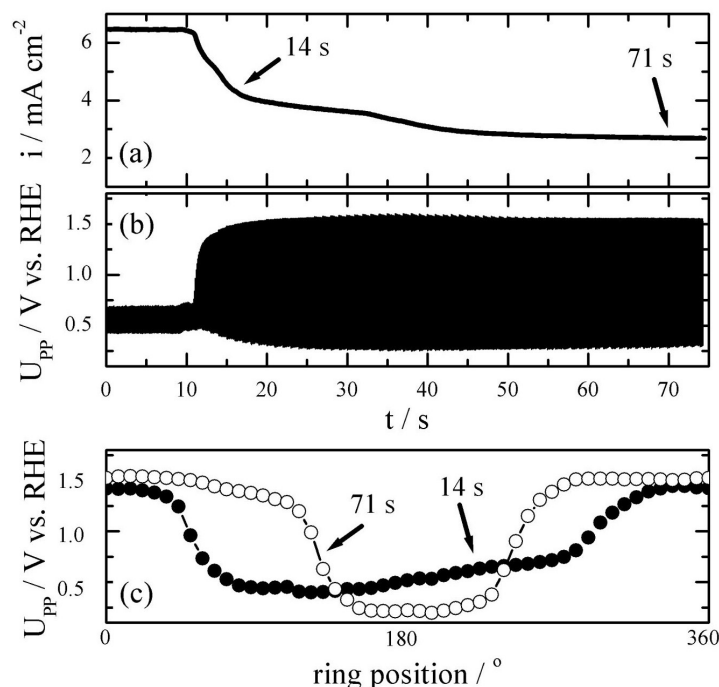


Figure 8.7: Emergence of stationary structures during the autonomous active/passive transition in the Pt|H₂SO₄|H₂ bistable system when subjected to strong NGC. (a) i , and (b) U_{PP} profiles as a function of time. (c) Snapshots of the U_{PP} profile along the WE at 14 (full circles) and 71 s (open circles). The applied voltage was 1.59 V. Here the distance between the plane of the WE and the tip of the Haber-Luggin capillary RE was set to 3 mm and under these conditions $R_c/R_\Omega \approx 0.4$. Electrolyte: 1.0 mM H₂SO₄ saturated with H₂. Rotation rate of the electrode $\omega = 20$ Hz. After Grauel and Krischer [41].

Noteworthy is the fact that the electrode potential in the active domain is approximately 0.2 V less positive than that of the homogeneous active state (i.e., the state which exists up to $t = 10$ s in Figure 8.7 (a) and (b)). Since the HOR has a negligible rate on a Pt(O)_x surface, the observed decrease in current results from the shrinking of the active domain.

The mechanism underlying the emergence of this stationary pattern results from the interplay between the two different spatial couplings acting in the system and can be summarized as follows. The desynchronizing effect of the NGC leads to an increase of ϕ_{DL} in regions where its value exceeds the average value of the electrode potential, $\langle \phi_{\text{DL}} \rangle$, and to a decrease of ϕ_{DL} in regions where its value is smaller than the average $\langle \phi_{\text{DL}} \rangle$. Furthermore,

the migration coupling broadens the interface between neighboring active and passive domains and leads to an Ostwald ripening. As a result, each state consists of just one active and one passive domain [27]. Hence, the formation of stationary potential walls reflects the equalization between the migration (stabilizing) and the negative global (destabilizing) couplings [27, 41].

8.4 TRAPPED OSCILLATIONS

The complex spatiotemporal patterns observed in region 2, cf. Figures 8.2 (a) and (c), result from a combination of the two different patterns discussed so far in this chapter: (a) the oscillatory patterns observed in region 1, Figure 8.2, which are linked to the oscillatory $\text{Pt|H}_2\text{SO}_4, \text{Cl}^-, \text{Cu}^{2+}|\text{H}_2$ system; and (b) the stationary patterns already present in the bistable $\text{Pt|H}_2\text{SO}_4|\text{H}_2$ system and illustrated in Figure 8.7. It was discussed in chapter 2 that oscillations in the (HN-NDR) $\text{Pt|H}_2\text{SO}_4, \text{Cl}^-, \text{Cu}^{2+}|\text{H}_2$ system are due to the specific potential dependence of the adsorption isotherms of Cl^- and Cu^{2+} . The adsorption of chloride ions occurs at more positive potentials, whereas copper adsorbs at less positive potentials. The $\text{Pt|H}_2\text{SO}_4|\text{H}_2$ system is of the N-NDR type and the stationary structures result from the interaction between the NGC and bistability between active and passive states.

The interaction between these two instabilities result in the trapping of oscillations or pulses between potential walls. Figure 8.8 shows (a) the formation of the self-organized potential walls in the (N-NDR) $\text{Pt|H}_2\text{SO}_4|\text{H}_2$ system [41] and (b) the ‘composite’ spatiotemporal patterns in the (HN-NDR) $\text{Pt|H}_2\text{SO}_4, \text{Cl}^-, \text{Cu}^{2+}|\text{H}_2$ system resulting from the superposition between ‘pre-organized’ potential walls and the oscillatory spatiotemporal patterns already present in region 1. Note that the patterns resulting from the interaction between the platinum oxide covered domain and the oscillatory structures of the $\text{Pt|H}_2\text{SO}_4, \text{Cl}^-, \text{Cu}^{2+}|\text{H}_2$ system and shown in Figure 8.8 (b) are stable and thus intrinsically different from those transient patterns depicted in chapter 7 (see Figure 7.3).

The pattern shown in Figure 8.8 (b) can be viewed as two consecutive pattern forming ‘events’. First the electrode surface pre-organizes in a sense that two domains are formed. Then, a symmetry breaking occurs within the active domain, i.e., the oxide free portion of the WE. Hence, the occurrence of the trapped oscillations shown in Figure 8.8 (b) results from the interplay between two different operating mechanisms: the N-NDR resulting from the

oxide formation that prepares the potential walls and the oscillatory HN-NDR that allows oscillations to occur in the active domain.

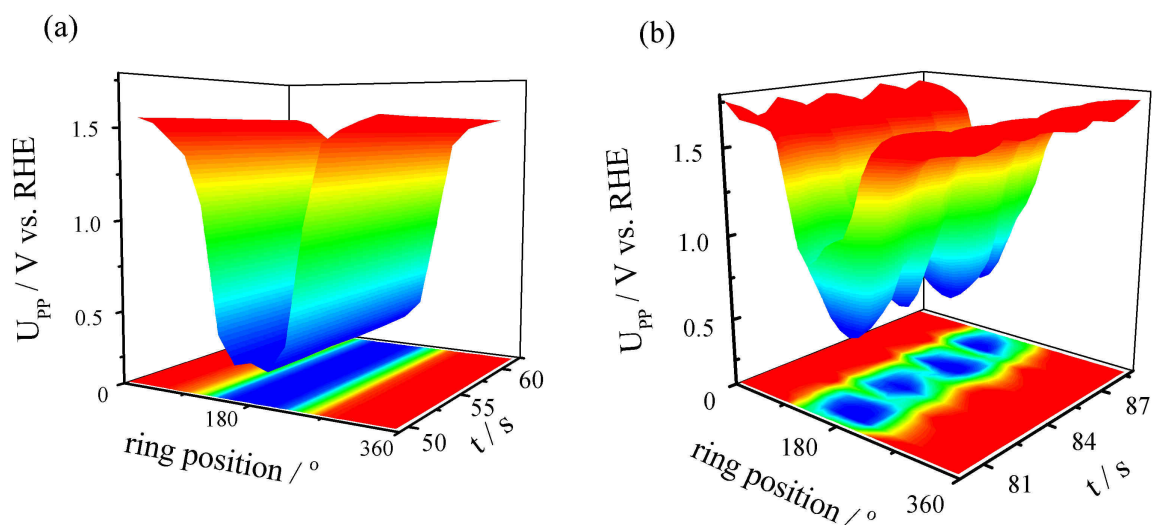


Figure 8.8: Three-dimensional representation of the interfacial potential distribution ($U_{pp}(x,t)$) as a function of time and angular position for the (a) Pt|H₂SO₄|H₂ bistable system, and (b) Pt|H₂SO₄,Cl⁻,Cu²⁺|H₂ oscillatory system. Data shown in (a) are the same as those given in Figure 8.7 (b) (after Grauel and Krischer [41]). In (b) $U = 1.49$ V, and the remaining experimental conditions are given in Figure 8.2.

Potentiostatic experiments in region 2 of Figure 8.2 were carried out. For applied voltages between 1.14 and 1.24 V, the walls were not completely stable, and small changes in the domain sizes were observed. From 1.25 to 1.53 V, however, no changes in the relative sizes of active and passive domains for a certain applied voltage were observed, and patterns were very stable. The full set of stationary experiments is given in Figure 8.9 for selected applied voltages inside this region. Shown is the spatiotemporal distribution of the interfacial potential together with the respective time series of the global current.

As apparent in all spatiotemporal space-time plots shown in Figure 8.10, in this parameter interval the electrode splits into two different regions, an active and a passive one. Furthermore, higher values of the applied voltage favor the growth of the passive (red) state on the expense of the active state (blue/green).

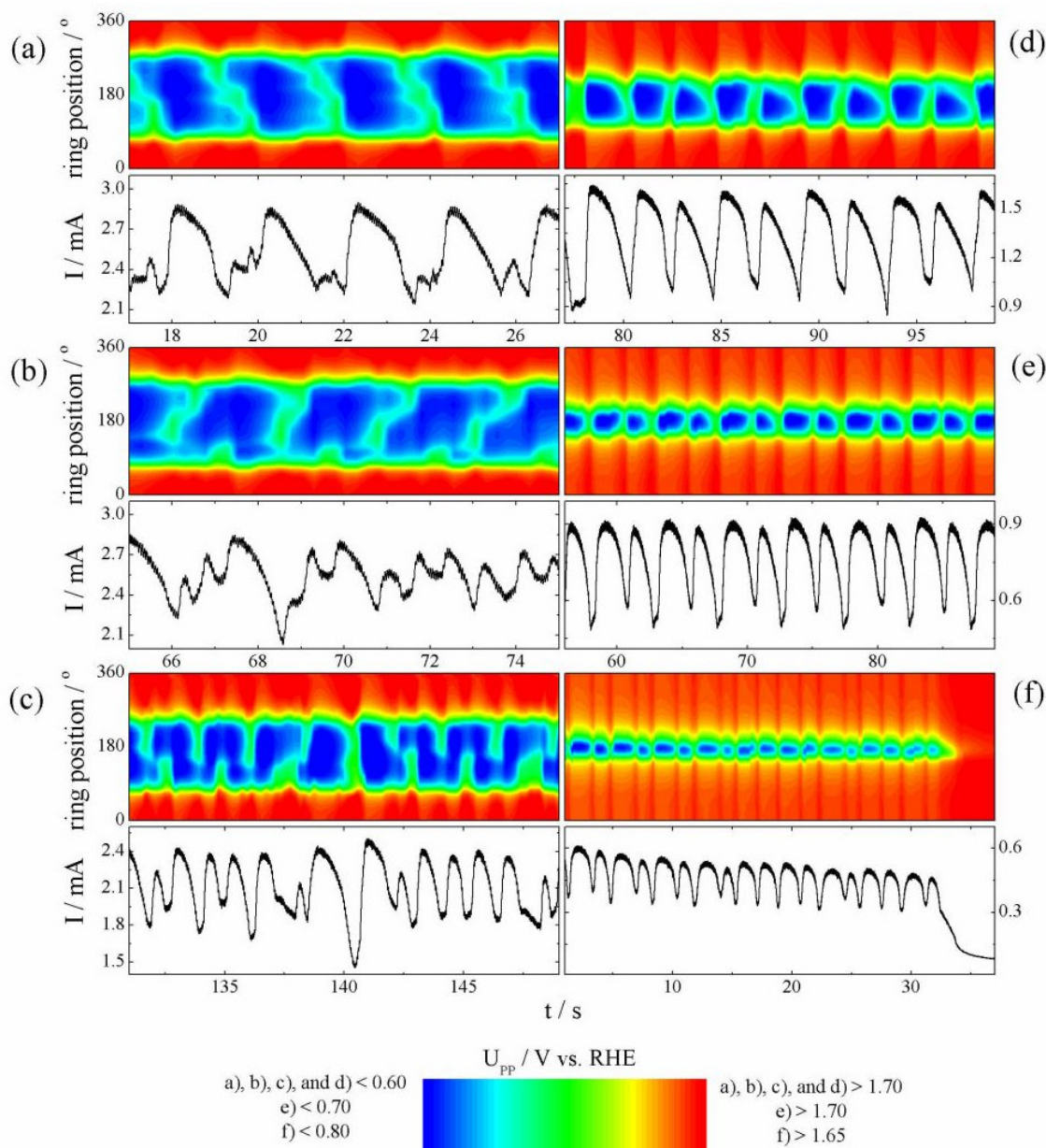


Figure 8.9: (a) Position-time plots of the interfacial potential distribution ($U_{PP}(x,t)$) and the respective global current time series for different values of the externally applied voltage, U : (a) and (b) 1.29 V, (c) 1.39 V, (d) 1.44 V, (e) 1.49 V, and (f) 1.54 V. The remaining experimental conditions are given in Figure 8.2.

The first set of structures depicted in Figure 8.9 is the one obtained at the lowest value of the applied voltage (plates (a) and (b)). Initially (plate (a)), the spatiotemporal evolution of the interfacial potential resembles a clockwise traveling pulse in the active portion of the WE. This state, however, evolves and, after ca. 40 s (plate (b)), the pulse spontaneously changes its direction and propagates in a counter clockwise fashion. It should be stressed that the

pattern inside the active region evolves in time, whereas no changes of the relative domain sizes are observed at a fixed applied voltage.

Recalling the behavior prevailing in region *I* (cf. Figure 8.2), where a pulse travels continuously along the ring, it is clear that the presence of the potential walls prevents the pulse from rotating around the entire ring. In this case, the pulse is trapped inside the active area, emerging at one end and being extinguished at the other end. Thus, the emergence of the self-organized potential walls changes the boundary conditions to which the pulse has to adjust from being periodic to being of the Dirichlet-type, i.e., the pulse faces a boundary with a nearly constant high potential value (a potential wall). These walls prevent it from propagating continuously along the ring electrode.

Increasing the applied voltage ($U = 1.39$ V, plate (c)) cluster-like structures are observed inside the active domain, i.e., the oscillatory domain is divided into two different regions, each region oscillating nearly in-phase and the two regions possessing a strong anti-phase character. Cluster-like behavior is known to arise from the presence of global coupling [190, 194, 195, 198-200, 204, 225] as already discussed in chapter 7.

The cluster-like dynamics described in the previous paragraph was observed when the active domain occupied about 56 % of the WE. When further increasing the applied voltage the width of the oscillating (active) domain shrinks, and only one domain survives for $U > 1.41$ V. Now, the entire active domain oscillates almost in-phase, cf. Figures 8.9 (d) and (e). Still, the oscillations are not simple periodic. Instead, the pattern approximately repeats every second oscillation, which also shows up in the time series of the global current. At $U = 1.54$ V, the size of the oscillating domain shrinks below a critical size, and the system attains a homogeneous, passive (red) state as depicted in Figure 8.9 (f).

Two additional effects caused by the oscillations in the active region are apparent in Figure 8.10 and worth mentioning. The first one concerns the oscillations of the interfacial potential within the passive (red) domain. Obviously, the oscillations in the active domain also enforce a slight periodic variation of the passive domain. The second point concerns the breathing of the potential walls. Clearly the interfaces between active and passive domains are not stationary in time. Rather, the passive domain tends to invade the active zone when the potential in the oscillating domain attains its highest value (green colored). Furthermore, three different forms of this breathing of the domain boundaries (potential walls) are

observed. Symmetric breathing is observed if there is only one oscillating domain (Figures 8.9 (d)–(f)); asymmetric breathing in the case of traveling pulses (Figures 8.9 (a) and (b)); and finally, an apparently desynchronized breathing is observed in the irregular cluster-like state shown in Figure 8.9 (c).

The continuous change of the relative domain sizes of active and passive areas with the externally applied voltage allows for studying pattern formation within the active area as a function of the domain size. In the example presented here, pulse-type motion is found for the largest domains. For smaller domains, there is apparently not sufficient space for the pulse to develop, and the system slips into the cluster-like state. The transition to the quasi-homogeneously oscillating state (from plates (c) to (d) in Figure 8.9) allows for extracting a critical system size for pattern formation, in this case it is of the order of magnitude of about 50 % of the WE length or ca. 4.7 cm.

8.5 CONCLUDING REMARKS

Besides pulses [47, 78, 221-224] and cluster-like [190, 194, 195, 198-200, 204, 225] patterns, which are known as typical examples of patterns arising from the presence of global coupling, it was shown in this chapter that NGC can bring about new nonequilibrium patterns. The complex patterns observed comprise spatiotemporal oscillating structures that are trapped between self-organized potential walls. It was shown that those patterns are observed in the presence of NGC and result from the interaction between the oscillatory patterns observed in the (HN-NDR) $\text{Pt}|\text{H}_2\text{SO}_4, \text{Cl}^-, \text{Cu}^{2+}|\text{H}_2$ system and stationary structures already present in the bistable $\text{Pt}|\text{H}_2\text{SO}_4|\text{H}_2$ system.

The patterns reported should not be restricted to the very system under consideration. Indeed, similar phenomena can be expected to occur in most HN-NDR systems, since in these systems generally only part of the N-NDR is hidden, implying that an N-NDR region follows the HN-NDR region as in most electrocatalyzed oxidation reactions of organic molecules [132]. This feature in connection with the NGC was identified as the source of the hierarchy of the unusual patterns.

The interaction of two features stemming from the interfacial kinetics, namely an N-NDR and an HN-NDR, and the NGC originating from the control of the electrochemical reaction, may give rise to a hierarchy of spatial symmetry breakings. This is especially

surprising since global coupling tends to give rise to structures with a wavelength that is equal to the system's size, as it is the case for the stationary domains, standing-wave or anti-phase oscillations and also the traveling pulses of Figure 8.3. Patterns such as those presented in Figure 8.9 reveal that global coupling might not only support structures that are far from being describable by simple (stationary or oscillating) spatial modes with $n = 1$, but also allow for nested spatial (and temporal) symmetry breakings of the emerging domains. In this respect, the discussed mechanism should be a universal route leading to a sub-structuring of space in systems that experience a global coupling and possess at least two adjacent regions in parameter space which exhibit distinct dynamical instabilities.